The electronic band structure of quasi-one-dimensional van der Waals semiconductors: The effective hole mass of ZrS_3 compared to TiS_3

Hemian Yi[1*], Simeon J. Gilbert[2*], Alexey Lipatov[3], Alexander Sinitskii[3,4], Jose Avila[1], Jehad Abourahma[3], Takashi Komesu,[2] Maria C. Asensio[5], and Peter A. Dowben[2]

[1]Synchrotron SOLEIL and Université Paris -Saclay, L'Orme des Merisiers, BP48, 91190 Saint-Aubin, France
[2]Department of Physics and Astronomy, University of Nebraska-Lincoln, Lincoln, NE 68588-0299, U.S.A.
[3]Department of Chemistry, University of Nebraska-Lincoln, Lincoln, NE 68588-0304, U.S.A.
[4]Nebraska Center for Materials and Nanoscience, University of Nebraska-Lincoln, Lincoln, NE 68588-0298, U.S.A.
[5]Materials Science Institute of Madrid (ICMM), Spanish Scientific Research Council (CSIC), Valencia Institute of Materials Science (ICMUV), MATINEE: CSIC Associated Unit-(ICMM-ICMUV Valencia University), E-28049 Cantoblanco, Madrid, Spain.

[*]These authors contributed equally to this work.

The band structure of the quasi-one-dimensional transition metal trichalcogenide ZrS_3(001) was investigated using nanospot angle resolved photoemission spectroscopy (nanoARPES) and compared to the band structure of TiS_3(001). We find that ZrS_3, like TiS_3, is strongly n-type with the top of the valence band ~1.9 eV below the Fermi level, at the center of the surface Brillouin zone. The nanoARPES spectra indicate that the top of the valence band of the ZrS_3(001) is located at $\overline{\Gamma}$. The band structure of both TiS_3 and ZrS_3 exhibit strong in-plane anisotropy, which results in a larger hole effective mass along the quasi-one-dimensional chains than perpendicular to them.

Keywords: Transition metal trichalcogenides, ZrS_3, effective mass, angle-resolved photoemission

The transition metal trichalcogenides (TMTs) are an emerging class of 2D materials that are receiving increasing amounts of attention due to their quasi-1D nature. In TMTs with a MX_3 composition (M= Ti, Zr, Hf, Ta; X= S, Se, Te), MX_3 trigonal prisms are covalently bound to form quasi-1D chains [1-14]. These chains are formed into 2D sheets via the van der Waals-like bonds between chains. This makes it possible to cleave the TMTs along the 1D chains which provides superior edge termination when compared to other 2D materials [1,2,4,5]. Additionally, the TMTs' quasi-1D nature gives rise to highly anisotropic optical and electrical and properties such as a preferred charge transport direction [7-10]. When combined, these attributes make the TMTs suitable for scaling to sub-10 nm widths [2,4,5] while avoiding both the short channel effects present in conventional electronics and the edge scattering effects [15-25] that plague other 2D materials.

Among the TMTs, TiS_3 has received the most attention due to a favorable band gap (~1 eV) [3,8,11,26-28] and its high predicted electron mobility (~10,000 $cm^2V^{-1}s^{-1}$) [3], although it is increasingly evident that phonon effects act to significantly reduce mobility [6]. Other semiconducting TMTs have received more limited attention, while TaS_3 [4,29,30] and $ZrTe_3$ [5], for example, are metallic. Higher Z value TMTs are expected to exhibit significant spin-orbit coupling [12,31] which is desirable for the next generation spintronic devices [32-35]. Despite this, research on the electronic properties and band structure of higher Z value TMTs is far from complete. There exist experimental band structure measurements of the region near the top of the valence band for both TiS_3(001) [8] as well as $ZrSe_3$ and $HfSe_3$ [12], but only limited information has been reported for ZrS_3(001) [12]. In the case of ZrS_3, there are a handful of theoretical band structure calculations [9-11,13,14]. The experimental effective hole mass, along the high

symmetry directions of $\overline{\Gamma}$ to $\overline{Y}$ and $\overline{\Gamma}$ to $\overline{B}$, along and perpendicular to the chain direction, has not been compared for TiS_3(001) and ZrS_3(001).

Nano-whiskers of ZrS_3 were synthesized by the reaction of metallic zirconium with sulfur vapor in vacuum-sealed quartz ampules at 800 °C, as described elsewhere [36,37]. Nano-whiskers of TiS_3 were grown by the reaction of metallic titanium with sulfur vapor in vacuum-sealed quartz ampules at 550 °C as described in our prior works [2,8,38]. The crystals of TiS_3 and ZrS_3 were characterized by X-ray diffraction (XRD) measurements in air at room temperature using a Rigaku Smart Lab diffractometer equipped with a Cu Kα source, λ = 1.5406 Å. Our XRD analysis indicates that the TiS_3 nanowhiskers conform to a monoclinic structure, with space group: $P2_1/m$, as illustrated in Figure 1, with TiS_3 lattice constants of a=4.9728(6) Å, b=3.4055(4) Å, c=8.8146(15) Å and a cant angle of β=97.56(1)°. These values remain in general agreement with earlier reported studies values of: a ranging from 4.849 to 4.973 Å, b from 3.326 to 3.433 Å, c from 8.714 to 8.815 Å, and β from 97.32 to 97.74° [7,8,39-42]. For ZrS_3, from XRD as shown in Figure 1c, the lattice constants are slightly larger with a = 5.1107(4) Å, b = 3.6179(2) Å, c = 8.9725(5), and β=97.64(1)° which are comparable to previously reported values for ZrS_3 ranging from 5.116 to 5.173 Å for a, 3.611 to 3.635 Å for b, 8.965 to 9.012 Å for c, and 97.13 to 97.46° for β [9,11,14,40,42-44].

Nanospot angle resolve photoemission spectroscopy (nanoARPES) was done at the Antares beamline of the synchrotron SOLEIL [45], Paris. Electron detection was achieved using a MBS deflection analyzer with an angular resolution of ~0.2° and energy resolution of ~10 meV. A spot size of ~120 nm allowed for the precise alignment and position on TiS_3 and ZrS_3 nano-whiskers [8,46,47] which were exfoliated *in situ* at a base pressure lower than 10^{-10} Torr. For

ZrS_3(001), the experimental valence band has been plotted after a taking the 2nd derivative of the experimental band structure, so as to illustrate the details of the band structure of ZrS_3(001).

The distances along the surface Brillouin zone, schematically shown in Figure 1b, from $\overline{\Gamma}$ to $\overline{B}$ and $\overline{\Gamma}$ to $\overline{Y}$ are determined by the lattice constants a and b. The corresponding distances in reciprocal space from $\overline{\Gamma}$ to $\overline{B}$ and $\overline{\Gamma}$ to $\overline{Y}$ for ZrS_3(001) are approximately 0.615 $Å^{-1}$ and 0.868 $Å^{-1}$, respectively, as indicated in Figure 2. This leads to a smaller surface Brillouin zone than is observed for TiS_3(001), 0.632 $Å^{-1}$ ($\overline{\Gamma}$ to $\overline{B}$) and 0.923 $Å^{-1}$ ($\overline{\Gamma}$ to $\overline{Y}$), which is also indicated in Figure 2.

Figure 2 shows the nanoARPES spectra along the high symmetry directions, from $\overline{\Gamma}$ to $\overline{Y}$ (parallel to the 1D chains) and from $\overline{\Gamma}$ to $\overline{B}$ (perpendicular to the chains), for both TiS_3 and ZrS_3, which are in general agreement with the calculated density of states [8,9-11,13,14]. The experimental electronic band structure is consistent with valence states of S 3*p* character, with only a limited admixture contribution of the Zr 4*d* states. In particular, the highest occupied states are derived from antibonding hybrid states of Π^*_g symmetry, with contributions from the 3p states of the sulfur and the Zr 5*p* and 4*d* states, while the first empty states have an antibonding σ^*_u character, with a S 3p and Zr 4d and 5p character [8,9-11,13,14].

Along both high symmetry directions, in the experimental band structure of TiS_3(001) determined by angle resolved photoemission, the top of the valence band is dominated by a single band centered at $\overline{\Gamma}$ (Figure 2a-b and 3a-b). The top of the valence band in TiS_3 lies ~1.0 eV below the Fermi level, as previously noted [8], which is consistent with an n-type semiconductor [1,6,7,37,46] with a band gap of ~1 eV [3,11,26,28].

For ZrS_3(001), multiple bands can be seen near the top of the valence region, in the experimental band structure of ZrS_3(001), determined by angle resolved photoemission. Along $\overline{\Gamma}$ to $\overline{Y}$ (Figure 2c), two bands, centered at $\overline{\Gamma}$, can be seen at binding energies of ~2-3 eV below the Fermi level. These bands have also been reported in a prior angle-resolved photoemission study of ZrS_3(001) [12]. In the $\overline{\Gamma}$ to $\overline{B}$ direction (Figure 2d), two bands, one centered at $\overline{\Gamma}$ and one centered between $\overline{\Gamma}$ and $\overline{B}$, can be seen at roughly 1.9 eV and 2.1 eV below the Fermi level, respectively. Given that ZrS_3(001) is expected to have a band gap of ~1.8 to 2.1 eV [9-11,14,40,49-52], the placement of the top of the valence band ~1.9 eV below the Fermi level is consistent with the strongly n-type character of ZrS_3 [48,51-53]. The two bands, observed at the top of the ZrS_3(001) valence band along $\overline{\Gamma}$ to $\overline{B}$, have been predicted by theory [9-11,13,14]. The same in-plane anisotropy is clearly demonstrated by the constant energy contours and close-in of the electronic band spectra along the high symmetric directions in TiS_3 and ZrS_3 indicated in Figure 4.

These experimental band structure measurements of ZrS_3(001) tend to indicate that the top of the valence band is at $\overline{\Gamma}$, which differs from the calculated band structure predictions [9-11,13,14], and the expectation that ZrS_3 is an indirect gap semiconductor [9-11,14,47,48]. Prior measurements have shown ZrS_3 to have an indirect optical band gap of ~2 eV [47,48] and a direct optical band gap between 2.0 and 2.8 eV [31,47-49]. The bottom of the conduction band, in ZrS_3, is expected to occur at either the Γ [11,13,14] or Z [9,10] Brillouin zone critical points. Meaning that if the valence band maximum actually occurs at $\overline{\Gamma}$, ZrS_3 could be a direct band gap semiconductor. Although, there are theoretical band structure calculations that have predicted that the difference between the indirect and direct bandgaps become increasingly negligible as the size shrinks from bulk to monolayer [11]. Among the theoretical band structure calculations for

ZrS_3(001) [9-11,13,14], the experimental band structure measurements shown here most closely resembles the calculated band structure for monolayer ZrS_3, under 2% biaxial tensile strain [14], in which the biaxial strain is predicted to result in an indirect to direct band gap transition. At this point, the situation might become better clarified with band structure calculations for both the surface and bulk of ZrS_3(001).

As is evident in Figure 2 and Figure 4, both TiS_3(001) (Figure 2a,b) and ZrS_3(001) (Figure 2c,d) show significant anisotropy along the surface Brillouin zone. This means that along the high symmetry lines of these trichalcogenides, the effective hole masses will differ. At the top of the valence band, the hole effective mass in TiS_3(001) is -0.95 ± 0.09 m_e from $\overline{\Gamma}$ to $\overline{Y}$ and -0.37 ± 0.1 m_e from $\overline{\Gamma}$ to $\overline{B}$, as noted elsewhere [8]. The measured hole effective mass for ZrS_3(001) is -0.87 ± 0.09 m_e from $\overline{\Gamma}$ to $\overline{Y}$, slightly less than a previously reported value of 1.0 m_e [12]. Along $\overline{\Gamma}$ to $\overline{B}$, for ZrS_3(001), the measured hole effective mass at the top of the valence band is 0.49 ± 0.2 m_e. Figure 3 illustrates the fittings with these effective hole masses to experimental band structure at the top of the valence band for TiS_3(001) (Figure 3a,b) and ZrS_3(001) (Figure 3c,d). The ratio of the hole effective mass along $\overline{\Gamma}$ to $\overline{Y}$ vs. $\overline{\Gamma}$ to $\overline{B}$ is 1.8:1 for ZrS_3(001), less than the hole effective mass ratio of 2.6:1 along the high symmetry directions for TiS_3(001), although the experimental uncertainties could significantly affect these ratios.

We have shown that ZrS_3(0001) nano-whiskers, like the previously reported TiS_3(001) [8], are strongly n-type. Superficially, the experimental band structures are similar. Like TiS_3(001), the hole effective mass for ZrS_3(001) is -0.87 ± 0.09 m_e from $\overline{\Gamma}$ to $\overline{Y}$, and 0.49 ± 0.2 m_e along $\overline{\Gamma}$ to $\overline{B}$, demonstrating that the measured hole effective mass at the top of the valence band has significant in-plane anisotropy.

Acknowledgements:

This research was supported by the National Science Foundation, through grants NSF-ECCS 1740136, as well as by the NCORE, a wholly owned subsidiary of the Semiconductor Research Corporation (SRC), through the Center for Antiferromagnetic Magneto-electric Memory and Logic (AMML), task i.d. 2760.002. The Synchrotron SOLEIL is supported by the Centre National de la Recherche Scientifique (CNRS) and the Commissariat à l'Energie Atomique et aux Energies Alternatives (CEA), France. This work was also supported by a public grant by the French National Research Agency (ANR) as part of the "Investissements d'Avenir" (reference: ANR-17-CE09-0016-05). The present research has been undertaken in the context of the Associated Unit MATINÉE of the CSIC (Spanish Scientific Research Council) created between the Materials Science Institute of Madrid (ICMM) and Valencia Institute of Materials Science (ICMUV).

References

[1] A. Lipatov, P.M. Wilson, M. Shekhirev, J.D. Teeter, R. Netusil, and A. Sinitskii, Nanoscale **7**, 12291 (2015).

[2] A. Lipatov, M.J. Loes, H. Lu, J. Dai, P. Patoka, N.S. Vorobeva, D.S. Muratov, G. Ulrich, B. Kästner, A. Hoehl, G. Ulm, X.C. Zeng, E. Rühl, A. Gruverman, P.A. Dowben, and A. Sinitskii, ACS Nano **12**, 12713 (2018).

[3] J. Dai and X.C. Zeng, Angew. Chemie - Int. Ed. **54**, 7572 (2015).

[4] T. A. Empante, A. Martinez, M. Wurch, Y. B. Zhu, A. K. Geremew, K. Yamaguchi, M. Isarraraz, S. Rumyantsev, E. J. Reed, A. A. Balandin and L. Bartels, Nano Lett. **19**, 4355 (2019).

[5] A. Geremew, M. A. Bloodgood, E. Aytan, B. W. K. Woo, S. R. Corber, G. Liu, K. Bozhilov, T. T. Salguero, S. Rumyantsev, M. P. Rao and A. A. Balandin, IEEE Electr. Dev. L. **39**, 735 (2018).

[6] M. Randle, A. Lipatov, A. Kumar, C.-P. Kwan, J. Nathawat, B. Barut, S. Yin, K. He, N. Arabchigavkani, R. Dixit, T. Komesu, J. Avila, M.C. Asensio, P.A. Dowben, A. Sinitskii, U. Singisetti, and J.P. Bird, ACS Nano **13**, 803 (2018).

[7] J.O. Island, M. Barawi, R. Biele, A. Almazán, J.M. Clamagirand, J.R. Ares, C. Sánchez, H.S.J. Van Der Zant, J. V. Álvarez, R. D'Agosta, I.J. Ferrer, and A. Castellanos-Gomez, Adv. Mater. **27**, 2595 (2015).

[8] H. Yi, T. Komesu, S. Gilbert, G. Hao, A.J. Yost, A. Lipatov, A. Sinitskii, J. Avila, C. Chen, M.C. Asensio, and P.A. Dowben, Appl. Phys. Lett. **112**, 1 (2018).

[9] A. Pant, E. Torun, B. Chen, S. Bhat, X. Fan, K. Wu, D.P. Wright, F.M. Peeters, E. Soignard, H. Sahin, and S. Tongay, Nanoscale **8**, 16259 (2016).

[10] X. Wang, K. Wu, M. Blei, Y. Wang, L. Pan, K. Zhao, C. Shan, M. Lei, Y. Cui, B. Chen, D. Wright, W. Hu, S. Tongay, and Z. Wei, Adv. Electron. Mater. **5**, 1900419 (2019).

[11] Y. Jin, X. Li, and J. Yang, Phys. Chem. Chem. Phys. **17**, 18665 (2015).

[12] D. Pacilé, M. Papagno, M. Lavagnini, H. Berger, L. Degiorgi, and M. Grioni, Phys. Rev. B - **76**, 155406 (2007).

[13] Q. Zhao, Y. Guo, Y. Zhou, Z. Yao, Z. Ren, J. Bai, and X. Xu, Nanoscale **10**, 3547 (2018).

[14] M. Li, J. Dai, and X.C. Zeng, Nanoscale **7**, 15385 (2015).

[15] X. Blase, C. Adessi, B. Biel, A. Lopez-Bezanilla, M.-V. Fernández-Serra, E.R. Margine, F. Triozon, and S. Roche, Phys. Status Solidi **247**, 2962 (2010).

[16] V.K. Dugaev and M.I. Katsnelson, Phys. Rev. B **88**, 235432 (2013).

[17] E.R. Mucciolo and C.H. Lewenkopf, J. Phys. Condens. Matter **22**, 273201 (2010).

[19] M. Wimmer, İ. Adagideli, S. Berber, D. Tománek, and K. Richter, Phys. Rev. Lett. **100**, 177207 (2008).

[20] J. Wurm, K. Richter, and İ. Adagideli, Phys. Rev. B **84**, 075468 (2011).

[21] O. V Yazyev, Reports Prog. Phys. **73**, 056501 (2010).

[22] M.Y. Han, J.C. Brant, and P. Kim, Phys. Rev. Lett. **104**, 056801 (2010).

[23] S.A. Jensen, R. Ulbricht, A. Narita, X. Feng, K. Müllen, T. Hertel, D. Turchinovich, and M. Bonn, Nano Lett. **13**, 5925 (2013).

[24] Y.-J. Shi, J. Lan, E.-J. Ye, W.-Q. Sui, and X. Zhao, Eur. Phys. J. B **87**, 251 (2014).

[25] Yinxiao Yang and R. Murali, IEEE Electron Device Lett. **31**, 237 (2010).

[26] I.J. Ferrer, M.D. Maciá, V. Carcelén, J.R. Ares, and C. Sánchez, Energy Procedia **22**, 48 (2011).

[27] I.J. Ferrer, J.R. Ares, J.M. Clamagirand, M. Barawi, and C. Sánchez, Thin Solid Films **535**, 398 (2013).

[28] J.O. Island, M. Buscema, M. Barawi, J.M. Clamagirand, J.R. Ares, C. Sánchez, I.J. Ferrer, G.A. Steele, H.S.J. van der Zant, and A. Castellanos-Gomez, Adv. Opt. Mater. **2**, 641 (2014).

[29] M. A. Stolyarov, G. X. Liu, M. A. Bloodgood, E. Aytan, C. L. Jiang, R. Samnakay, T. T. Salguero, D. L. Nika, S. L. Rumyantsev, M. S. Shur, K. N. Bozhilov and A. A. Balandin, Nanoscale **8**, 15774 (2016).

[30] G. X. Liu, S. Rumyantsev, M. A. Bloodgood, T. T. Salguero, M. Shur and A. A. Balandin, Nano Letters **17**, 377 (2017).

[31] W. Schairer and M.W. Shafer, Phys. Status Solidi **17**, 181 (1973).

[32] P.A. Dowben, C. Binek, K. Zhang, L. Wang, W.-N. Mei, J.P. Bird, U. Singisetti, X. Hong, K.L. Wang, and D. Nikonov, IEEE J. Explor. Solid-State Comput. Devices Circuits **4**, 1 (2018).

[33] N. Sharma, C. Binek, A. Marshall, J. P. Bird, P. A. Dowben and D. Nikonov, "Compact Modeling and Design of Magneto-Electric Transistor Devices and Circuits," *2018 31st IEEE International System-on-Chip Conference (SOCC)*, Arlington, VA, USA, IEEE Explore (2018) 146-151; doi: 10.1109/SOCC.2018.8618494; URL: http://ieeexplore.ieee.org/stamp/stamp.jsp?tp=&arnumber=8618494&isnumber=8618478

[34] D.E. Nikonov, C. Binek, X. Hong, J.P. Bird, K.L. Wang, and P.A. Dowben, US 10,361,292 B2 (2019).

[35] N. Sharma, J. P. Bird, Ch. Binek, P. A. Dowben, D. Nikonov, and A. Marshall, "Evolving Magneto-electric Device Technologies", Semiconductor Science and Technology (2019), in the press

[36] D. S. Muratov, A. R. Ishteev, D. A. Lypenko, V. O. Vanyushin, P. Gostishev, S. Perova, D. S. Saranin, D. Rossi, M. Auf der Maur, G. Volonakis, F. Giustino, P. O. Å. Persson, D. V. Kuznetsov, A. Sinitskii, and A. Di Carlo, ACS Applied Materials & Interfaces **11**, 48021 (2019).

[37] D. S. Muratov, V. O. Vanyushin, N. S. Vorobeva, P. Jukova, A. Lipatov, E. A. Kolesnikov, D. Karpenkov, D. V. Kuznetsov, and A. Sinitskii, Journal of Alloys and Compounds **815**, 152316 (2020).

[38] Q. Cui, A. Lipatov, J.S. Wilt, M.Z. Bellus, X.C. Zeng, J. Wu, A. Sinitskii, and H. Zhao, ACS Appl. Mater. Interfaces **8**, 18334 (2016).

[39] S.J. Gilbert, A. Lipatov, A.J. Yost, M.J. Loes, A. Sinitskii, and P.A. Dowben, Appl. Phys. Lett. **114**, 101604 (2019).

[40] L. Brattås, A. Kjekshus, J. Krogh-Moe, J. Songstad, Å. Pilotti, Acta Chem. Scand. **26**, 3441 (1972).

[41] S. Kikkawa, M. Koizumi, S. Yamanaka, Y. Onuki, S. Tanuma, Phys. Status Solidi Appl. Mater. Sci. **61**, K55 (1980).

[42] S. Furuseth, L. Brattås, A. Kjekshus, Acta Chem. Scand. A **29**, 623 (1975).

[43] H. Jin, D. Cheng, J. Li, X. Cao, B. Li, X. Wang, X. Liu, and X. Zhao, Solid State Sci. **13**, 1166 (2011).

[44] L. Huang, K. Tang, Q. Yang, G. Shen, and S. Jia, Mater. Res. Bull. **39**, 1083 (2004).

[45] J. Avila, I. Razado-Colambo, S. Lorcy, B. Lagarde, J. L. Giorgetta, F. Polack, and M. C. Asensio, J. Phys. Conf. Ser. 425, 192023 (2013).

[46] J. Avila and M. C. Asensio, Synchrotron Radiat. News 27, 24 (2014).

[47] J. Avila, I. Razado, S. Lorcy, R. Fleurier, E. Pichonat, D. Vignaud, X. Wallart, and M. C. Asensio, Sci. Rep. 3, 2439 (2013).

[48] N. V. Morozova, I. V. Korobeinikov, K. V. Kurochka, A.N. Titov, and S. V. Ovsyannikov, J. Phys. Chem. C **122**, 14362 (2018).

[49] S. Kurita, J.L. Staehli, M. Guzzi, and F. Levy, Phys. B **105**, 169 (1981).

[50] G. Perluzzo, S. Jandl, and P.E. Girard, Can. J. Phys. **58**, 143 (1980).

[51] E. Flores, J.R. Ares, I.J. Ferrer, and C. Sánchez, Phys. Status Solidi - Rapid Res. Lett. **10**, 802 (2016).

[52] O. Gorochov, A. Katty, N. Le Nagard, C. Levy-Clement, A. Redon, and H. Tributsch, J. Electrochem.Soc. **130**, 1301 (1983).

[53] G. Perluzzo, A.A. Lakhani, and S. Jandl, Solid State Commun. **35**, 301 (1980).

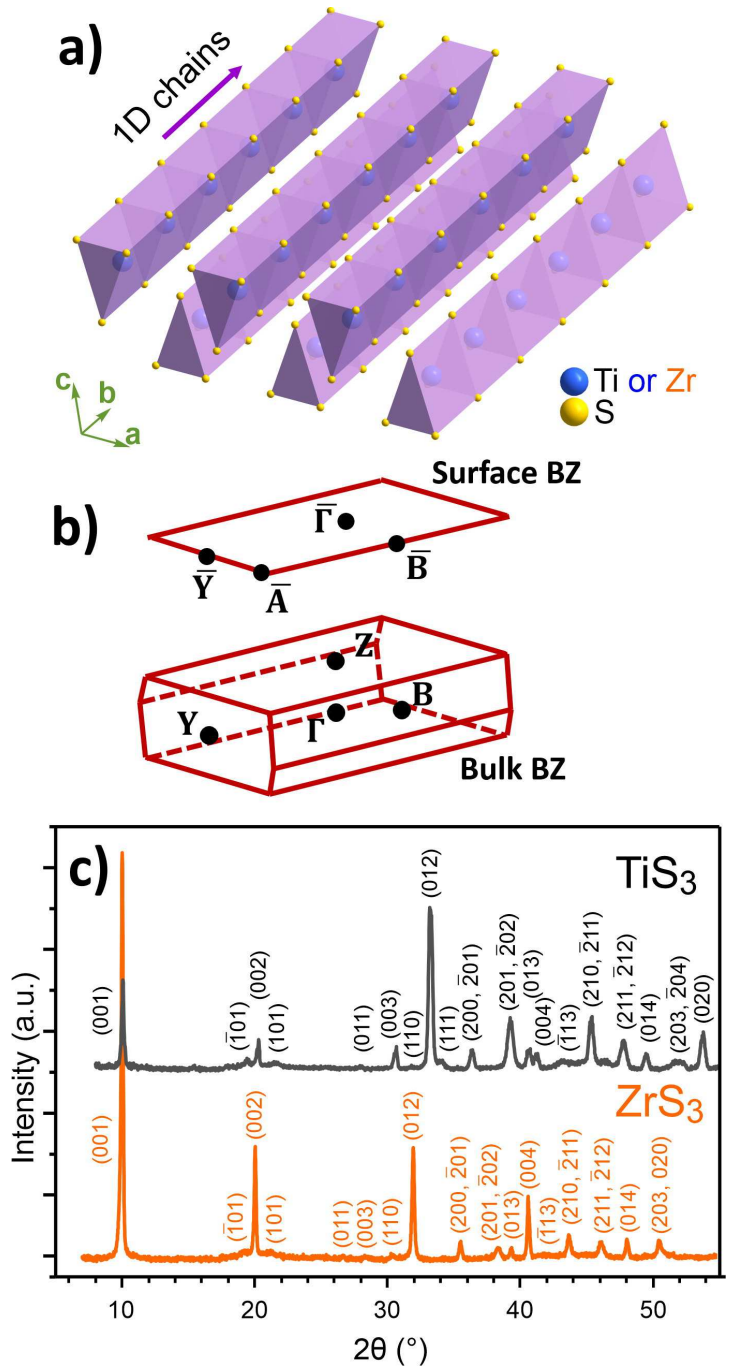

Figure 1. a) A scehmatic of the structure of a bilayer of TiS_3 or ZrS_3. b) The surface and bulk Brillouin zones for TiS_3(001) or ZrS_3(001). c) The XRD pattern taken from the TiS_3 and ZrS_3 powders.

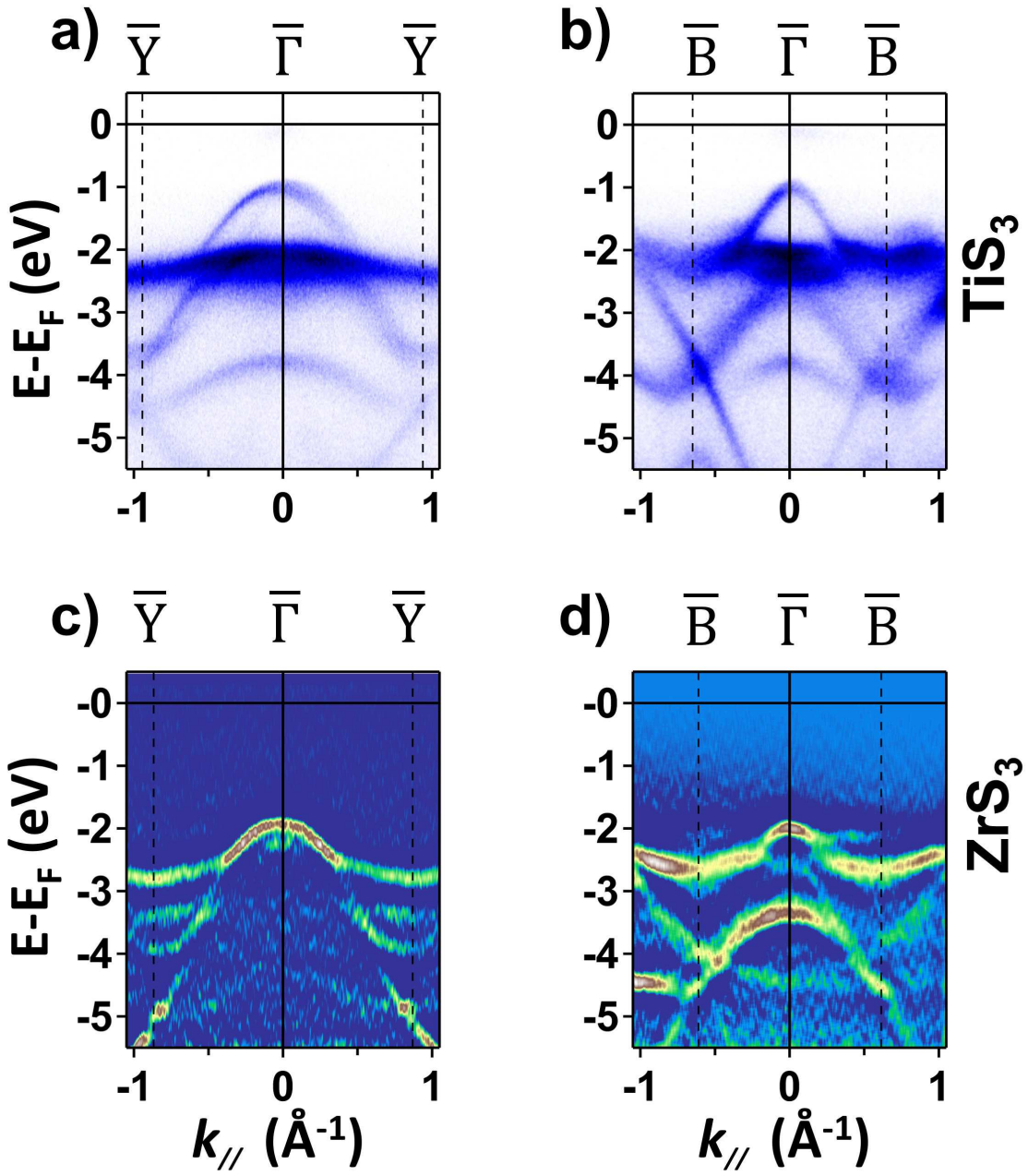

Figure 2. The experimental band structure of TiS_3(001) (a,b) and ZrS_3(001) (c,d) along the high symmetry directions of $\overline{\Gamma}$ to $\overline{Y}$ (a,c) and $\overline{\Gamma}$ to $\overline{B}$ (b,d), as derived from nanoARPES. a) and b) were adapted from [8]. c) and d) are plots of the top of the valence band, after a taking the 2nd derivative of the experimental band structure, so as to illustrate the details of the band structure of ZrS_3(001).

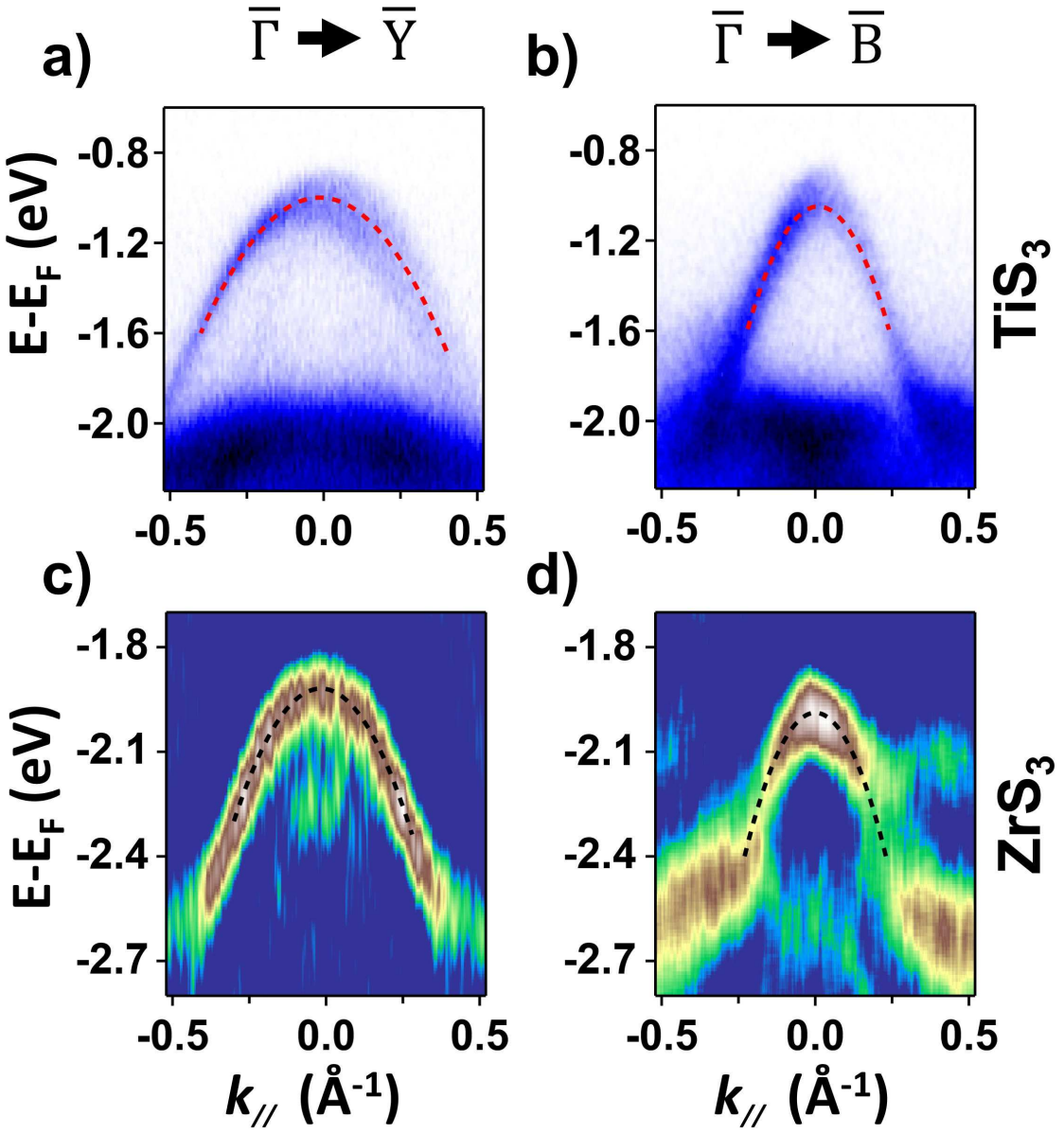

Figure 3. The top of the valence band for TiS_3(001) (a,b) and ZrS_3(001) (c,d) along the high symmetry directions of $\overline{\Gamma}$ to $\overline{Y}$ (a,c) and $\overline{\Gamma}$ to $\overline{B}$ (b,d). Dotted lines represent fitting curves used to calculate the effective hole masses of a) -0.95 ± 0.09 m_e, b) -0.37 ± 0.1 m_e, c) -0.87 ± 0.09, and d) 0.49 ± 0.2 m_e.

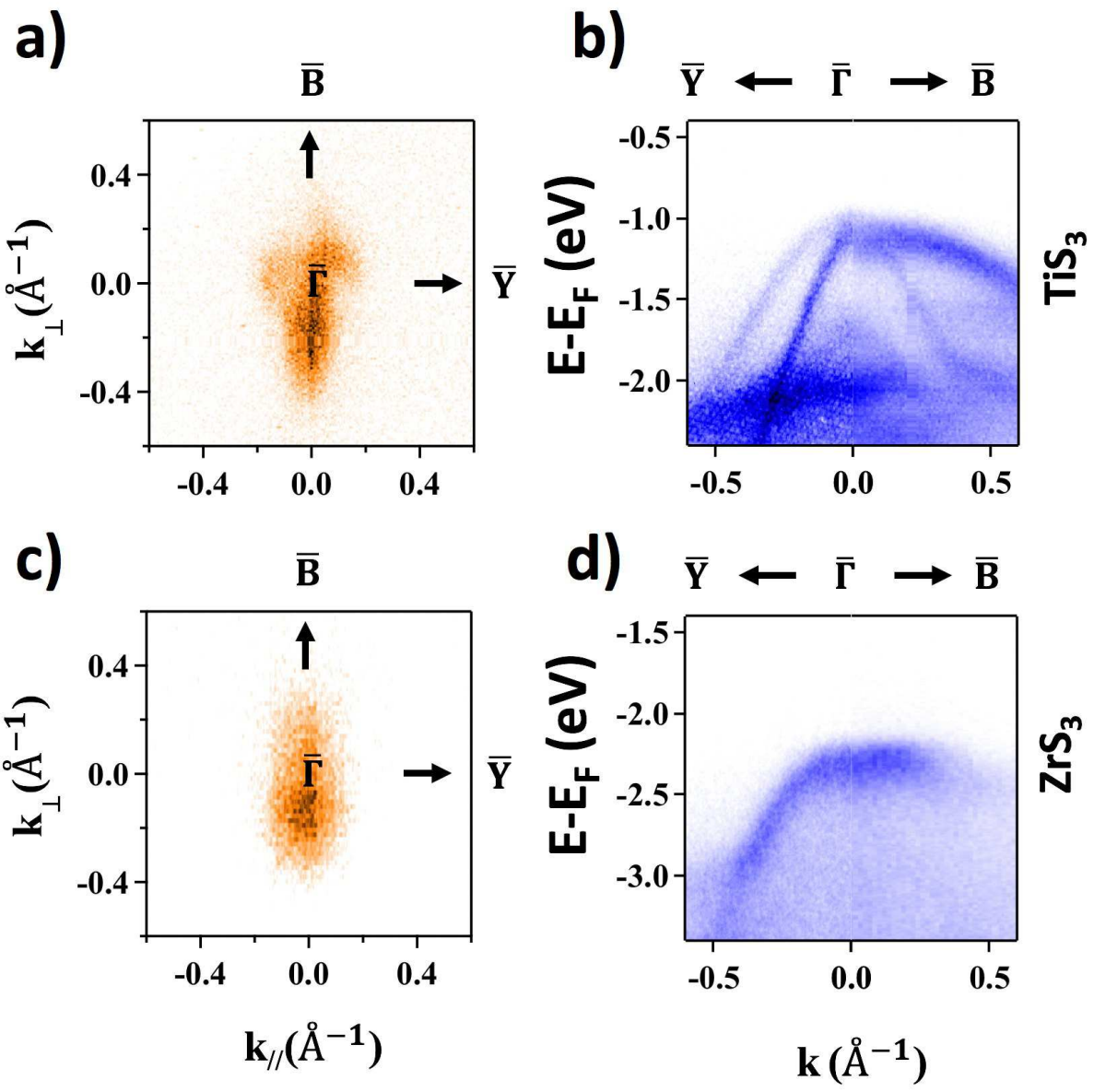

Figure 4. The constant energy contours (a,c) near the top of the valence band and close-in of the electronic band spectra along the high symmetric directions $\overline{\Gamma}$-$\overline{B}$ and $\overline{\Gamma}$-$\overline{Y}$ directions for TiS_3 (b) and ZrS_3 (d). The results for TiS_3 is in panels (a) and (b) and for ZrS_3 in panel (c) and (d).